OPEN ACCESS
IOP Publishing
Measurement Science and Technology
Meas. Sci. Technol. **36** (2025) 115902 (12pp)
https://doi.org/10.1088/1361-6501/ae10d4

Directional emissivity characteristics of yttria-stabilised zirconia thermal barrier coatings

Matthew Stokes and Thomas Povey*

Department of Engineering Science, University of Oxford, Parks Road, Oxford OX1 3PJ, United Kingdom

E-mail: thomas.povey@eng.ox.ac.uk

Received 12 June 2025, revised 26 September 2025
Accepted for publication 8 October 2025
Published 20 November 2025

Abstract

The use of infrared (IR) thermography techniques is increasingly common in gas turbine research. A current area of interest, for example, is the assessment of component overall cooling effectiveness using IR full-surface temperature measurements. To achieve high accuracy in such experiments, it is necessary to know the emissivity characteristics of the surfaces under test. For many surfaces, there is high view-angle dependence of emissivity for observation angles above 55°. Two common surface types used in gas turbine experiments are thermal barrier coatings (TBCs) and high-emissivity paint. In this paper, we present experimental measurements of the directional emissivity characteristics for a range of yttria-stabilised zirconia (YSZ) TBC samples, and a range of high-emissivity paints sprayed onto a smoother metal (copper) surface (as used for *in-situ* calibration assemblies). TBC samples were taken from engine parts. Semi-physical curve fits to the data are explicitly provided. The purpose of this study is to provide accurate directional emissivity characteristics that can be used by the experimental community.

Keywords: yttria-stabilised zirconia, directional emissivity, thermal barrier coatings, emissivity, infrared

Nomenclature

Romans

a, b, c	Curve fit coefficients [-]
c_p	Specific heat capacity [J kg^{-1} K^{-1}]
$E_{\lambda, T}$	Spectral emissive power [W m^{-2} Sr^{-1}]
h_{in}	Convective heat transfer coefficient inside test enclosure [W m^{-2} K^{-1}]
h_{nc}	Convective heat transfer coefficient of external test enclosure surfaces [W m^{-2} K^{-1}]
k	Thermal conductivity [W m^{-1} K^{-1}]
k_{Roh}	Thermal conductivity of Rohacell [W m^{-1} K^{-1}]
k_{S}	Equivalent sand grain roughness [μm]
k_{TP}	Thermal conductivity of thermal paste [W m^{-1} K^{-1}]
q_{cam}	Total incident radiation on IR camera in spectral band of detector [W m^{-2} Sr^{-1}]
q_{w}	Radiation emitted by target surface that is incident on IR camera in spectral band of detector [W m^{-2} Sr^{-1}]
q_{R}	Radiation emitted by relatively isothermal surroundings [W m^{-2} Sr^{-1}]
q'_{R}	q_{R} reflected off target surface and incident on IR camera in spectral band of detector [W m^{-2} Sr^{-1}]
R_{a}	Mean surface roughness [μm]
T_{amb}	Surrounding environmental temperature [K]
T_{b}	Blackbody temperature [K]

* Author to whom any correspondence should be addressed.

T_{bb}	Blackbody calibrator surface effective blackbody temperature [K]
T_{Cu}	Copper baseplate temperature [K]
T_w	Wall (surface) temperature [K]
z	Layer thickness [μm]
z_{TP}	Thermal paste layer thickness [μm]

Greeks

β_{T_b}	Bias uncertainty in T_b [K]
β_{ϵ_w}	Bias uncertainty in ε_w [-]
β_θ	Bias uncertainty in θ [deg]
ε	Emissivity [-]
ε_F	Emissivity of Fresnel (optically smooth) surface [-]
ε_w	Emissivity of target surface [-]
θ	View angle [deg]
θ_{Cu}	View angle with respect to copper baseplate [deg]
λ	Wavelength [μm]
ρ	Density [kg m^{-3}]
ρ_w	Reflectivity of target surface [-]
σ	Stefan–Boltzmann constant [W m^{-2} Sr^{-1} K^{-4}]
τ	Transmittance [-]
τ_w	Transmittance of target surface [-]

Subscripts

bb	Blackbody calibrator surface
Cu	Copper
ep	Epoxy
F	Fresnel (optically smooth) surface
In	Inconel
Roh	Rohacell
TP	Thermal paste
w	Surface (wall)

Abbreviations

APS	Air plasma sprayed
EB-PVD	Electron-beam particle vapour deposition
IR	Infrared
LWIR	Long-wavelength IR range
NGV	Nozzle Guide Vane
PTC	Positive temperature coefficient
RTD	Resistance temperature detector
TBC	Thermal barrier coating
TRL	Technology Readiness Level
YSZ	Yttria-stabilised zirconia

1. Introduction and literature review

The use of IR thermography techniques is increasingly common in gas turbine research to capture two-dimensional surface (wall) temperature measurements non-intrusively. To recover the surface temperature (T_w) from the blackbody temperature measured by an IR camera (T_b), it is necessary to know the directional emissivity characteristics of the surface, $\epsilon_w(\theta)$, where θ is the view angle (the angle between the surface normal and a line connecting the surface to the camera). The view-angle variation of ϵ_w can become significant for $\theta > 55°$.

Two common surface types encountered in gas turbine IR experiments are thermal barrier coatings (TBCs) and high-emissivity paints sprayed onto metal surfaces. We study yttria-stabilised zirconia (YSZ) TBC of two different types: air plasma sprayed (APS) TBC, with a layered (splatted) microstructure with pores aligned parallel to the surface; and electron-beam particle vapour deposition (EB-PVD) TBC, with a columnar structure aligned perpendicular to the surface. EB-PVD TBC coatings are generally applied in thinner (50–250 μm thickness) layers, offer higher resistance to mechanical stress and thermal shock, and have lower surface roughness (mean surface roughness $R_a = 1.3$–1.6 μm) and higher thermal conductivity ($k = 1.2$–1.6 W m^{-1} K^{-1}). APS TBC coatings are generally applied in a thicker layer (200–600 μm thickness), and have higher surface roughness ($R_a =$ 4–5 μm) and lower thermal conductivity ($k = 0.8$–1.1 W m^{-1} K^{-1}). High-emissivity paints are often applied by aerosol spray in a relatively thin layer (10–50 μm thickness), have similar thermal conductivity to TBC ($k = 0.5$–1.5 W m^{-1} K^{-1}) and surface roughness in the range $1.5 < R_a < 5.5$ μm.

YSZ TBC has favourable spectral emissivity and reflectivity characteristics in engine applications, where the peak of the blackbody spectrum (wavelength of $\lambda = 2.4$ μm at $T_w =$ 1200 K) coincides with a region of low emissivity (and therefore absorption) and higher reflectivity. These, in combination, reduce heat load due to radiation (lower absorption). Taking the surface temperature of a typical cooled nozzle guide vane (NGV) as 1200 K in the engine environment (see, for example [1],), and 300 K in a high-technology readiness level (high-TRL) experimental facility environment (see, for example [2]), and taking the spectral emissivity ($\epsilon_w(\lambda)$), reflectivity ($\rho_w(\lambda)$) and transmittance ($\tau_w(\lambda)$) characteristics of typical YSZ TBCs from [3], we can plot characteristics (with the wavelength) of background radiation intensity and emissivity for both environments. This is shown in figure 1.

Consider first the engine condition; the peak spectral blackbody emissive power occurs at a wavelength of 2.4 μm. At this wavelength, YSZ TBC has high reflectivity ($\rho_w(\lambda = 2.4\ \mu m) = 0.638$) and low emissivity ($\epsilon_w(\lambda = 2.4\,\mu m) = 0.132$). The remaining 23.0% of incident radiation is transmitted through the TBC ($\tau_w(\lambda = 2.4\ \mu m) =$ 0.230) and interacts with the underlying substrate (a bond coat or the metal component). Now consider the typical rig condition ($T_w = 300$ K). Peak emission is at $\lambda = 9.7$ μm, at which wavelength YSZ TBC is opaque ($\tau_w(\lambda = 9.7\ \mu m) = 0$), with very high emissivity ($\epsilon_w(\lambda = 9.7\,\mu m) = 0.944$) and very low reflectivity ($\rho_w(\lambda = 9.7\ \mu m) = 0.056$). This difference is relevant to the design of experimental IR measurement techniques.

Laboratory experiments using IR techniques to evaluate surface temperatures commonly use long-wavelength IR range (LWIR) cameras, which detect radiation in the range $7.5 < \lambda < 14$ μm. The integrating window of a typical uncooled microbolometer array (a microelectronic component commonly used to detect IR radiation in LWIR cameras) is indicated in figure 1. In typical laboratory conditions ($T_w = 300$ K), the LWIR range is well matched to the emitting spectral range and, fortuitously, in a range where the emissivity of YSZ TBC

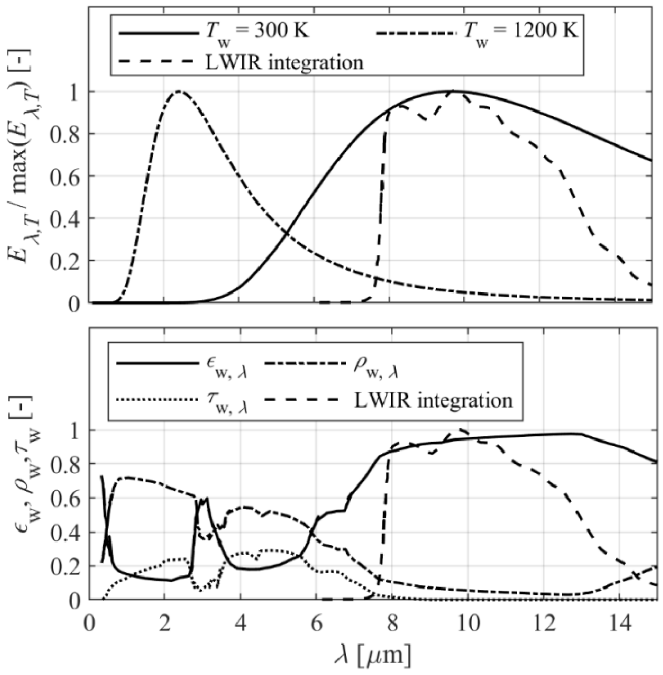

Figure 1. (top) Normalised emissive power at typical engine and rig wall temperatures as a function of the wavelength; (bottom) normal spectral emissivity, reflectivity and transmittance (data from [3]) as a function of the wavelength.

is also high (see figure 1): approximate average values over the integrating range of the camera are $\epsilon_w = 0.938$, $\rho_w = 0.060$, $\tau_w = 0.002$. This means that the total radiation received by the camera is dominated by radiation directly emitted from the target surface, and is not strongly affected either by reflected surrounding radiation or by the substrate temperature below the TBC (because $\tau_w \approx 0$). There are also no absorption bands for atmospheric gases (CO_2, H_2O) within the spectral range of the camera, allowing the air between the camera and the target to be considered a perfect transmitter ($\tau = 1$).

Although there are some limited data in the literature for normal and directional emissivity, reflectivity and transmittance of YSZ TBC [3–7], there are, as far as the authors know, no published data for YSZ TBC samples from typical engine components (same deposition process, same typical roughness, etc), nor data which are through-calibrations with typical LWIR cameras (accounting for integrating range, etc). Current open-literature measurements [3–7] have been conducted with laboratory-prepared samples and in facilities with IR spectrometers, giving detailed spectral emissivity and transmittance data. The emissivity and transmittance of TBC have been shown by these studies to be affected by many factors, including surface roughness, topcoat thickness, surface microstructure, chemical composition and view angle. With regard to directional emissivity, data reported in the open literature are typically the total emissivity (the integral over the full spectral range of the spectrometer used). Because the integration ranges of LWIR cameras would, in general, be different from the spectrometers used in such studies, it would be hard to translate published results to effective directional emissivity relationships for particular surface-camera pairings that are common in experimental work.

The purpose of the present study is to provide accurate directional emissivity through-calibrations for TBC samples from real turbine components paired with typical LWIR cameras. The results are of practical importance for temperature measurements in laboratory turbine experiments. We study TBC test coupons extracted from the airfoils (EB-PVD TBC) and endwalls (APS TBC) of nozzle guide vanes from a modern turbofan engine. We also study three types of high-emissivity paint commonly used in laboratory turbine experiments. Paint of various types was sprayed onto smooth metal (copper) coupons. We use an optical profilometer to characterise the surface roughness and coating thickness (from sectioned coupons) of each coupon. The directional emissivity characteristics of the coupons were measured in the range $0° \leqslant \theta \leqslant 85°$. We provide semi-physical curve fits to allow direct implementation of the measured directional emissivity characteristics in IR processing codes.

2. Basic physics of the problem

We now briefly discuss the fundamental physics of IR temperature measurement for real, non-blackbody, surfaces. Figure 2 shows a conceptual system in which an LWIR camera is being used to measure the temperature (T_w) of a wall. The wall has emissivity $\epsilon_w(\theta)$, and reflectivity $\rho_w(\theta)$. Here, θ is the angle from the surface normal. In this simplest system, there are no intermediate optics (windows) in-between the camera and the target surface. The target surface and camera are surrounded by radiating surfaces at an, assumed uniform, temperature, T_{amb}.

The IR camera measures the total incoming radiance, q_{cam}. Using a camera-lens-specific blackbody calibration, the equivalent blackbody temperature measured by the camera, T_b, is inferred from q_{cam}. The total incoming radiance, q_{cam}, is the sum of two terms: the radiation directly emitted by the target surface, q_w; and the component of surrounding radiation (q_R) reflected off the target surface, q'_R. That is, $q_{cam} = q_w + q'_R$. If the surrounding environment can be assumed to have a uniform equivalent blackbody temperature, this can be expressed as

$$\sigma T_b^4(\theta) = \sigma \epsilon_w(\theta) T_w^4 + \sigma \rho_w(\theta) T_{amb}^4 \quad (1)$$

where σ is the Stefan–Boltzmann constant, and T_{amb} is the equivalent blackbody temperature of the surroundings. If the surface is opaque (a good approximation for most laboratory experiments with TBC and over-painted surfaces) over the spectral band of the camera, $\rho_w(\theta) = 1 - \epsilon_w(\theta)$. To recover the true wall temperature from the equivalent blackbody temperature, we need to determine the radiative flux from the surrounding surfaces (q_R) and the emissivity and transmittance of the target surface. There are established solutions to the first part of this problem, namely, *in-situ* calibration techniques capable of determining q_R in environments with both uniform (see [8]) and non-uniform (see [9]) surrounding radiance. The second

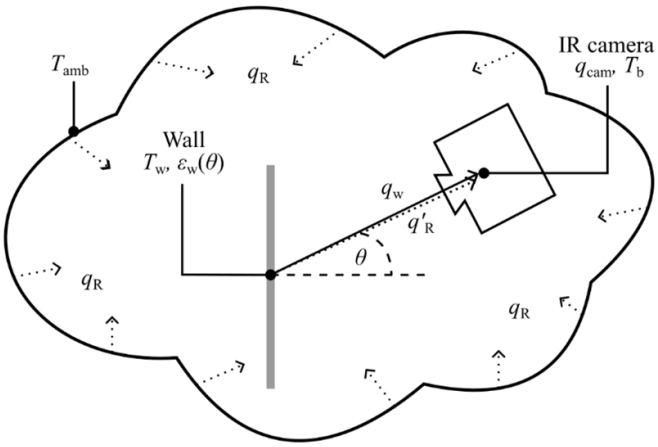

Figure 2. A schematic of a simple IR system for measurement of a wall temperature T_w.

part of this problem (determination of $\epsilon_w(\theta)$ and, by extension, $\rho_w(\theta)$, is the subject of this paper.

3. Experimental method

This section considers the details of the test sample preparation and characterisation, the test facility design and operation, the calculation of the observation angle and measurement of emissivity. We also consider the measurement bias uncertainty in the emissivity and observation angle.

3.1. Test coupon preparation and characterisation

In total, 13 coupons, ten YSZ TBC test coupons and three coupons coated with high-emissivity paints, were studied. A summary of the coupon descriptions, their thickness (z) and their equivalent sandgrain roughness height (k_S), is given in table 1. The ten TBC test coupons were spark eroded from a new (non-engine-deteriorated) nozzle guide vane from a modern turbofan engine. Seven EB-PVD coupons (coupons 1–7) were extracted from the (trailing vane) airfoil of the NGV pair. Three APS coupons (coupons 8–10) were extracted from the NGV endwalls. Three additional coupons (coupons 11–13) were of high-emissivity paint, directly over-sprayed onto the copper baseplate. These included: Autotek VHT black paint, a high-temperature-capable acrylic-based self-priming paint; RS matt black spray paint, a matt acrylic-based paint marketed for its high opacity; and NEXTEL Velvet 811-21, an acrylic-based paint marketed for its high-emissivity (up to 98%). For completeness, we note that the EB-PVD and APS TBC types have different chemical compositions, and the APS TBC has an intermediate MCrAlY bond coat between the topcoat and the metal substrate.

All coupons were cleaned of dielectric (used in the electrical discharge machining process) after machining, and then mounted onto a heated copper baseplate with a thin layer of high-thermal-conductivity epoxy. The surface roughness and thickness of the TBC or paint layers were characterised using optical profilometry (Alicona InfiniteFocus machine). For the surface roughness, three 500×500 μm areas per coupon were measured (the resolution is 0.1 μm). At each measurement location, the equivalent sandgrain roughness height (k_S) was calculated by following the methodology of Bons [10]. An average of the three measurements (per coupon) was taken. Thickness measurements were performed using the same equipment viewing coupon sections. The thickness was calculated by measuring the mean distance between the top of the underlying (metal) substrate and the exposed topcoat surface. For the APS TBC coupons, the thickness of the bond coat was subtracted from the measurement.

Table 1. A summary of coupon descriptions, coating thickness (z) and equivalent sandgrain roughness height (k_S).

Test coupon	Description	z (μm)	k_S (μm)
1	EB-PVD TBC	76	2.41
2	EB-PVD TBC	136	3.41
3	EB-PVD TBC	150	3.35
4	EB-PVD TBC	154	3.37
5	EB-PVD TBC	182	5.76
6	EB-PVD TBC	185	6.22
7	EB-PVD TBC	189	3.21
8	APS TBC	287	15.60
9	APS TBC	320	14.84
10	APS TBC	343	22.48
11	Autotek VHT black paint	12	4.66
12	RS matt black paint	22	5.49
13	NEXTEL Velvet paint	46	9.55

3.2. Test facility design and operation

A schematic of the test facility developed for this study is shown in figure 3. It consists of: a thick copper baseplate (5 mm thick) designed to maintain near-isothermal conditions; 13 coupons attached to (or over-sprayed on) the copper baseplate; an enclosure made of low thermal conductivity Rohacell foam ($k_{Roh} = 0.03$ W m^{-1} K^{-1}), designed to ensure near-isothermal conditions during the heating phase; a self-regulating PTC heater mounted (thin layer of thermal paste of thickness $z_{TP} = 0.2$ mm and conductivity

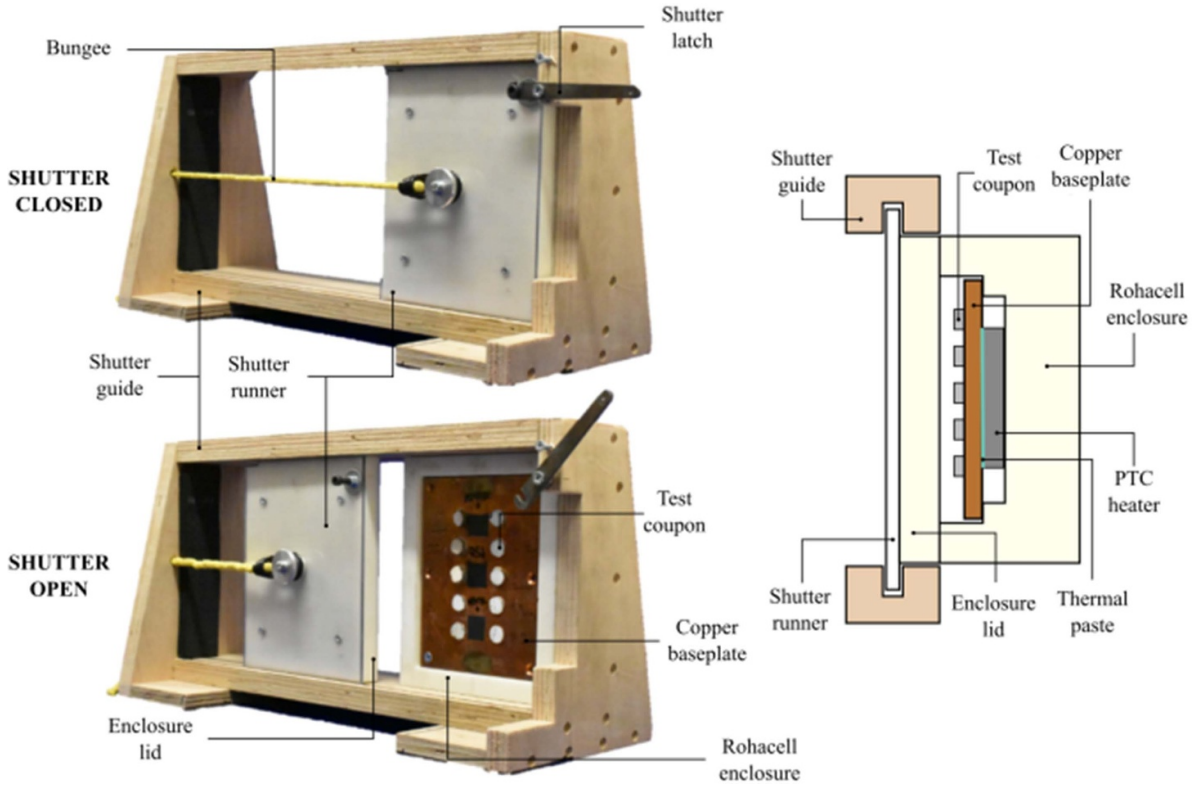

Figure 3. A schematic of the directional emissivity calibration system.

$k_{TP} = 6.5$ W m^{-1}K^{-1}) on the rear surface of the copper plate, capable of temperatures of around 105 °C; a fast-acting shutter system, which opens the enclosure shutter in less than 0.1 s.

The copper plate temperature (T_{Cu}) is monitored by three class-1 platinum RTDs (overall accuracy ±0.21 K at nominal PTC heater temperature). During operation, the plate and enclosure are heated until steady conditions are obtained (the typical change in T_{Cu} over 15 min is $\Delta T_{Cu} \leqslant 0.15$ K). A low-order thermal model was used to confirm that the outer wall temperature (T_w) of the coupons with highest thermal resistance was the same as the copper plate temperature to within 0.1 K. Therefore, after this heating period, all samples are isothermal at the nominal facility operating temperature ($T_w =$ 378 K). The data-acquisition averaging period was the 0.1 s period after the shutter was fully open. The thermal model (which included natural convection terms) was used to demonstrate that the coupons remained isothermal (in the through-wall direction) to within 0.1 K during this period. Further details of the thermal model are given in appendix A.

IR measurements were taken using two LWIR cameras: a MicroEpsilon TIM640 camera, and a FLIR A655sc camera. Further details, including the spectral ranges, are given in table 2. An in-house blackbody calibration was performed for both cameras using a CI-systems SR-800N blackbody surface (NIST traceable). We relate the raw camera output (an unsigned 16-bit integer proportional to the total radiation incident on the detector array in the spectral range of the camera) to T_b^4 with a linear best fit. The calibration was performed over the range 308 K $\leqslant T_b \leqslant$ 393 K.

Table 2. The IR camera specifications.

Camera	Spectral range (μm)	Frame rate (Hz)	Detector
MicroEpsilon TIM640	7.5–13	32	Uncooled microbolometer
FLIR A655sc	7.5–14	25	Uncooled microbolometer

The IR cameras were orbited around the central vertical axis of the copper baseplate in 5° increments in the range $0 \leqslant \theta_{Cu} \leqslant 85°$, where θ_{Cu} is the rotational angle of the camera about the vertical centreline of the copper plate. The distance between the axis of rotation and the camera was 0.5 m in all tests. The camera centreline was aligned for each position with an alignment guide marked onto the worksurface. The alignment guides were lines drawn from the vertical centreline of the copper baseplate to the camera tripod centre position. The test facility was bolted into the work surface to prevent movement between tests. The camera tripod was locked for all tests at the same vertical height.

3.3. Observation angle calculation

As not all coupons lie on the centreline of the copper plate, and as the target surface of most coupons is not exactly parallel to the copper plate surface (due to surface curvature, etc.), further correction is required to determine the local observation angle (θ) of each coupon from the rotational angle of the

camera about the vertical centreline of the copper plate (θ_{Cu}). A high-resolution 3D scan of the copper baseplate (and test facility) was performed using an Artec Space Spider. The point cloud produced by the scan has an accuracy of ± 0.05 mm. For each coupon, a 6 mm diameter circular region of interest was specified in the centre of the coupon, and the mean surface normal vector of the region of interest was calculated. Using this, for every camera rotational angle (θ_{Cu}), the local surface observation angle (θ) was calculated on a per-coupon per-test basis. Where necessary, to reduce error (to capture data at low θ for coupons close to the edges of the plate), the cameras were positioned at two vertical heights.

3.4. Emissivity calculation

Taking the approximation $\rho_{\mathrm{w}}(\theta) = 1 - \epsilon_{\mathrm{w}}(\theta)$ (transmissivity of zero) we can rearrange equation (1) in terms of the emissivity for each coupon. We get

$$\epsilon_{\mathrm{w}}(\theta) = \frac{T_{\mathrm{b}}^4(\theta) - T_{\mathrm{amb}}^4}{T_{\mathrm{w}}^4 - T_{\mathrm{amb}}^4} \tag{2}$$

where we recall that $T_{\mathrm{b}}(\theta)$ is the equivalent blackbody temperature measured by the camera, T_{w} is the surface temperature of the coupon and T_{amb} is the equivalent blackbody temperature of the surroundings. In our test, we take $T_{\mathrm{b}}(\theta)$ as the average over the central 6 mm diameter circle of our coupon, and we measure T_{amb} using a digital thermometer in the room (we have low sensitivity to background radiation in our experiment due to high coupon emissivity, and higher coupon temperature). In this formulation it is assumed that the surrounding surfaces are diffusely reflecting and uniformly radiant (overhead lighting and other heat sources were eliminated, and nearby reflective surfaces were covered).

3.5. Bias uncertainty

We now estimate the total bias uncertainty of measured (T_{b}, T_{w}, T_{amb}, and θ_{Cu}) and derived (ϵ_{w} and θ) quantities. All uncertainties are quoted to 95% confidence. For the derived quantities, a Monte Carlo analysis was used.

First consider the directly measured quantities. Here, T_{w} was measured using three class-1 platinum RTDs, each with a quoted uncertainty of ± 0.36 K at the nominal temperature. The bias uncertainty in the measured average temperature was therefore estimated to be $\pm 0.36/\sqrt{3} = \pm 0.21$ K, to 95% confidence. T_{amb} was measured using a digital thermometer with a manufacturer-quoted uncertainty of ± 1 K to 95% confidence. The bias uncertainty in the in-house calibrated blackbody temperature is a function of the accuracy, stability and uniformity of the blackbody calibration surface temperature T_{bb} (combined RMS error ± 0.2 K), the uncertainty of the emissivity of the calibration surface ($\epsilon_{\mathrm{bb}} = 0.99 \pm 0.01$) and the uncertainty in T_{amb}. A Monte Carlo analysis was used to estimate the bias uncertainty in the equivalent blackbody temperature measured by the camera (T_{b}). Perturbed variations of the original calibration dataset (T_{bb}, T_{atm} and ϵ_{bb}) are formed by adding offsets of appropriate magnitude (randomly sampled from Gaussian distributions of width appropriate to the corresponding bias error) to the underlying calibration datasets.

Table 3. Nominal values and associated bias uncertainties of measured variables.

Parameter	Bias uncertainty (95% confidence)	Nominal value
T_{w} [K]	± 0.21	378
T_{amb} [K]	± 1	290
T_{bb} [K]	± 0.2	308–393
ϵ_{bb}	± 0.01	0.99
T_{b} [K]	± 0.4	318–378
θ_{Cu} [°]	± 1	0–85
$[x,\ y,\ z]$ [mm]	± 0.05	—

The bias uncertainty in the equivalent blackbody temperature measured by the camera, $\beta_{T_{\mathrm{b}}}$, is defined as twice the standard deviation of the distribution of the perturbed calibration curves so formed. We obtain a value of $\beta_{T_{\mathrm{b}}} = \pm 0.4$ K to 95% confidence. The estimated uncertainty in θ_{Cu} at all camera positions was $\pm 1°$. The accuracy of the 3D scanned point cloud coordinates (i.e. $[x,\ y,\ z]$), used to calculate θ on an individual-coupon individual-view basis, was estimated as ± 0.05 mm to 95% confidence (manufacturer-quoted errors). The bias errors (95% confidence) and associated nominal values of the directly measured quantities are given in table 3.

Bias uncertainties for the derived quantities ϵ_{w} and θ ($\beta_{\epsilon_{\mathrm{w}}}$ and β_θ, respectively) were also calculated using Monte Carlo analysis. For ϵ_{w}, perturbed values of T_{b}, T_{w} and T_{amb} are picked from Gaussian distributions to calculate the output ϵ_{w} distribution. The uncertainty $\beta_{\epsilon_{\mathrm{w}}}$ is defined as twice the standard deviation of the resulting ϵ_{w} distribution. Separate simulations were performed across the range $0.5 \leqslant \epsilon_{\mathrm{w}} \leqslant 1$ (0.01 increments) to determine the worst-case bias uncertainty across this range. The resulting worst-case $\beta_{\epsilon_{\mathrm{w}}}$ was estimated to be ± 0.0143 (1.47% at $\epsilon_{\mathrm{w}} = 0.97$), to 95% confidence. To calculate β_θ, the Monte Carlo analysis considered the uncertainties in θ_{Cu} and the per-coupon per-view correction determined from the 3D scan. In each simulation, the 3D point cloud was perturbed by a common randomly generated offset of form $(\Delta x,\ \Delta y,\ \Delta z,)$ and with the standard deviation of the manufacturer-quoted scanner accuracy (0.05 mm to 95% accuracy). Here, θ_{Cu} was also randomly perturbed (bias error of $\pm 1°$), and θ was calculated for each coupon following the method described previously. Separate simulations were performed across the range $0° \leqslant \theta_{\mathrm{Cu}} \leqslant 85°$ in increments of $1°$ to determine the worst-case bias uncertainty across this range. The resulting bias uncertainty in θ was $\pm 1.28°$, to 95% confidence.

4. Results

We now discuss the experimentally determined directional emissivity characteristics (ϵ_{w} as a function of θ). The functional form for the fits is given by

$$\epsilon_{\mathrm{w}}(\theta) = \epsilon_{\mathrm{F}}(a, \theta) + be^{c\theta} \tag{3}$$

where $\epsilon_{\mathrm{F}}(a, \theta)$ is the Fresnel emissivity, and $be^{c\theta}$ is a term to correct for rough surfaces. With regard to fitting, a, b, c are

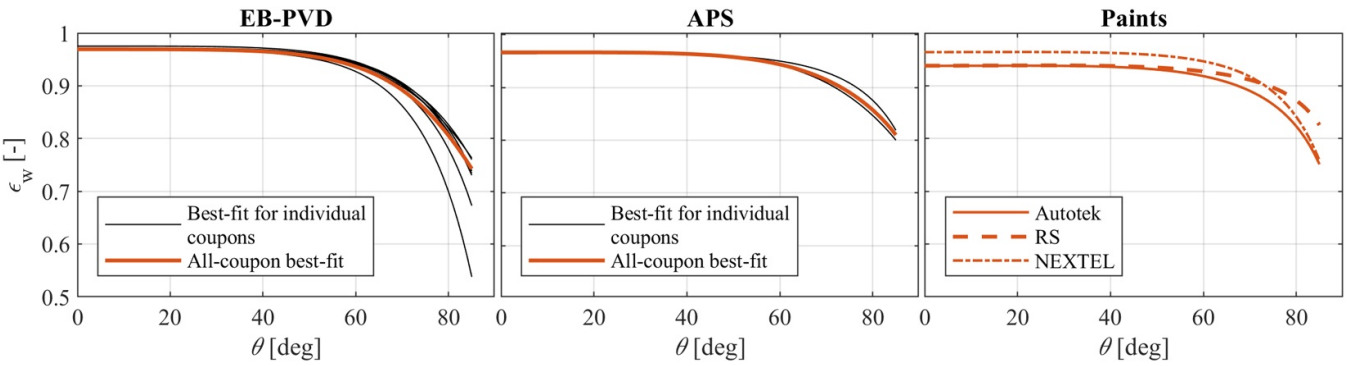

Figure 4. Best fits for individual coupons measured using the FLIR A665sc camera, and the best fit for all the coupons.

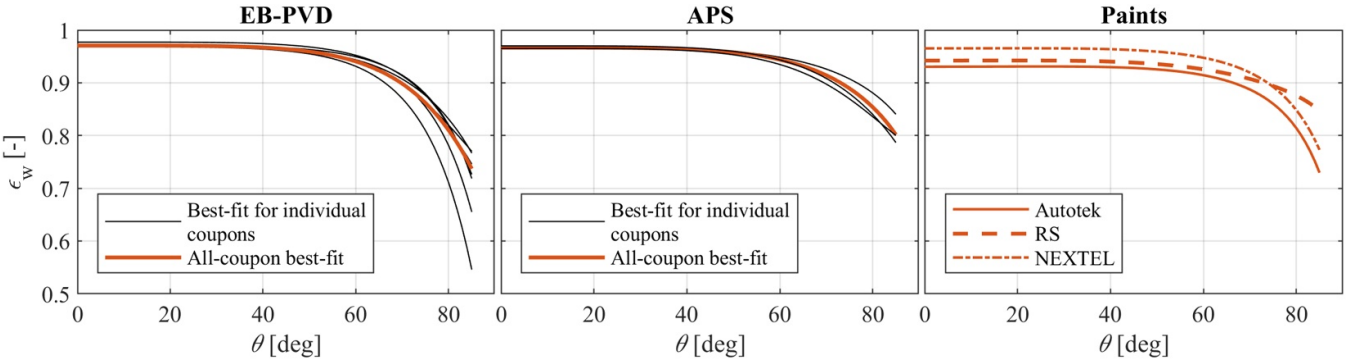

Figure 5. Best fits for individual coupons measured using the MicroEpsilon TIM640 camera, and the best fit for all the coupons.

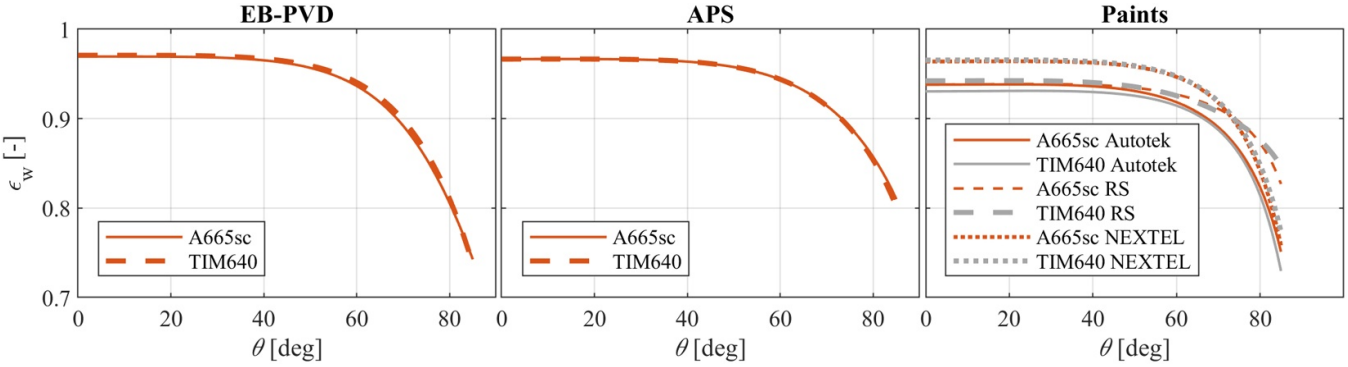

Figure 6. Comparison of the best fits for the FLIR A665sc and MicroEpsilon TIM640 cameras.

free constants determined by non-linear least squares fitting of the data in MATLAB. The physical basis for this form of equation is discussed in more detail in appendix B.

In figure 4 we show best-fit curves on a per-coupon basis, and for all coupons of a particular surface type, as measured using the FLIR A665sc camera. The left, middle and right frames show trends for EB-PVD TBC, APS TBC, and paints, respectively. For EB-PVD TBC and APS TBC surface types, multiple coupons were used for each surface type (see table 1). Best-fit curves on a per-coupon basis are shown with faint lines, and the overall best fit (for all coupons of a given surface type) as a bold line. Corresponding plots showing (almost identical) data collected with the TIM640 camera are shown in figure 5. A comparison between overall best-fit trends for data taken with the FLIR A665sc and TIM640 cameras is shown in figure 6. Deviation of individual data points from the overall best-fit trend (using data from both cameras) is shown in figure 7.

We now progress the analysis under three headings: measurement differences between cameras; individual-coupon variability; and summary directional emissivity characteristics.

4.1. Measurement differences between cameras

First consider the effect of measurement differences between cameras. Differences in the measured directional emissivity characteristics can arise due to variations in the integration

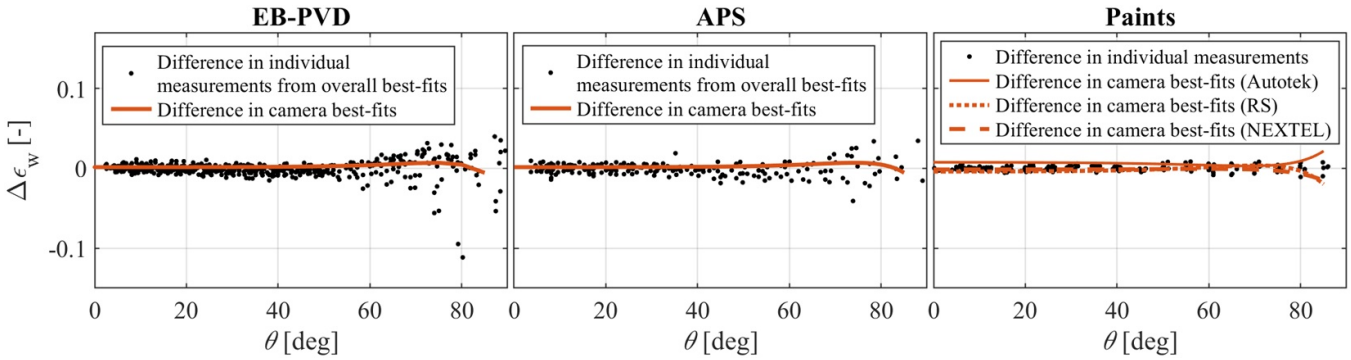

Figure 7. The differences in the best fits obtained using the FLIR A665sc camera and TIM640 cameras; scatter of individual ϵ_w measurements around the overall best fit (data from both cameras).

characteristics of the cameras, the bias uncertainties in the individual camera calibrations and uncertainties in individual experimental data points from which the best fits are formed. The all-coupon best-fit curves for the five surface types (two TBC types, three paint types) as measured by both cameras, are compared in figure 6. For a given surface type, the cameras deliver extremely similar calibrations: this is true for all five surface types. This is shown most clearly by looking at the differences in the best-fit ϵ_w characteristics, $\Delta\epsilon_w$, as functions of the angle. These are shown in figure 7. The average values of $\Delta\epsilon_w$ across the range $0° \leqslant \theta \leqslant 85°$ were 0.0022 for EB-PVD TBC and 0.0025 for APS TBC. The corresponding maximum values in this range were $\Delta\epsilon_w = 0.006$ and 0.009, respectively. For both sample types, the maximum difference between cameras is less than the bias uncertainty in emissivity ($\beta_{\epsilon_w} = 0.0143$). This suggests that the as-measured emissivities of both TBC types are insensitive to the integration characteristics of the LWIR cameras (for the two cameras used). For Autotek, RS matt and NEXTEL paints, the average values of $\Delta\epsilon_w$ across the range $0° \leqslant \theta \leqslant 85°$ were 0.007, 0.002, and 0.002, respectively. The corresponding maximum values were $\Delta\epsilon_w = 0.015$, 0.017 and 0.015, respectively. For each paint, the maximum difference occurs at $\theta = 85°$. When restricting the range to $\theta < 80°$, the maximum values of $\Delta\epsilon_w$ reduce to 0.009, 0.007 and 0.003 (within the bias uncertainty of the measurement). As we found for the TBC surfaces, the directional emissivity characteristics of the paint surfaces were insensitive to the integration characteristics of the LWIR cameras.

4.2. Individual-coupon variability

We now examine the measurement coupon variability for the five types of surfaces tested, i.e. the scatter around the best-fit curve. For the two TBC types, for which we tested several coupons of each type, we consider the coupon-to-coupon variability as well as the measurement coupon variability overall.

First consider the data for EB-PVD TBC. For this surface type we had seven coupons. First consider the coupon-to-coupon variability. This is shown by individual, per-coupon, lines of best fit, shown in figures 4 and 5. The data from the two cameras are very similar. For the 14 individual characteristics (i.e. particular coupon, particular camera) the mean (across 14 coupon–camera pairs) RMS deviation of data sets from their own characteristics was $\Delta\epsilon_w = 0.0044$ across the range $0° \leqslant \theta \leqslant 85°$. When restricting the range to $0° \leqslant \theta \leqslant 60°$, the mean RMS deviation falls to $\Delta\epsilon_w = 0.0036$. These are extremely small numbers, showing excellent agreement with the form of equation (3) for data acquired for individual coupons with an individual camera. Now, taking the RMS deviation of all data for EB-PVD TBC (all coupons, both cameras) from the overall best fit (data from all coupons and both cameras) we get values of $\Delta\epsilon_w = 0.0997$ and 0.0062 over the ranges $0° \leqslant \theta \leqslant 85°$ and $0° \leqslant \theta \leqslant 60°$, respectively. The deviation of all individual data points from the overall best fit is shown in figure 7. We have already noted that the measurement difference between cameras (the solid line in figure 7) is extremely small. RMS deviations from the overall best fit are approximately two times larger than RMS deviations from individual (per coupon, per camera) fits. These values are still sufficiently small so that the overall best fits are adequate in most problems. However, in situations where extremely high accuracy is required, it may be necessary to perform an individual calibration (specific surface, specific camera through-calibration).

For completeness we note three additional detailed points for the data for EB-PVD TBC. Firstly, there is generally increasing scatter of the data with increasing θ. This is, perhaps obviously, partly attributable to the increasing steepness of the $\epsilon_w(\theta)$ characteristic at high θ, which amplifies the impact of uncertainty in θ on the RMS deviation of individual coupons around the overall best-fit trend. Secondly, test coupons 1 and 7 (see table 1) have outlying trends (as measured by both cameras), particularly in the range $\theta > 60°$. Test coupons 1 and 7 are significantly smoother than average ($k_S = 2.41$ μm and $k_S = 3.21$ μm, respectively, compared to an average value of $k_S = 3.96$ μm), and there is a known positive correlation between surface roughness and emissivity, particularly at large θ (see [11]). This appears to explain the outlying trends. It is worth noting that data for test coupons 1 and 7 contribute significantly to the higher RMS deviations of all data from the overall best fit, particularly in the range $\theta > 60°$. As the NGV vane surfaces (the EB-PVD-coated part of the component)

can normally be viewed at relatively low θ (compared to the endwalls) in most test facilities, we conclude that EB-PVD-type TBC is suitably described by the global overall best-fit trend over the practical range of viewing angles. Finally, we note that all seven EB-PVD coupons have very similar normal emissivity ($\theta = 0°$) values, despite the significant range of TBC thicknesses covered by the coupons ($76 \leqslant z \leqslant 189$ μm; see table 1): indeed, all data are within the range of experimental uncertainty ($\beta_{\epsilon_w} = \pm 0.0143$). This is contrary to some previous studies (see, for example [3]), which have observed a reduction in normal emissivity with decreasing TBC thickness. We conclude that for EB-PVD of the type tested, normal emissivity is fairly insensitive to thickness for the typical range of thicknesses encountered in turbine airfoil coating applications.

Now we consider the data for APS TBC. For this surface type we had three coupons. First consider the coupon-to-coupon variability. This is shown by individual, per-coupon, lines of best fit, shown in figure 4 (FLIR A665sc camera) and figure 5 (TIM640 camera). The data from the two cameras are very similar. For the six individual characteristics (i.e. particular coupon, particular camera) the mean (across six coupon–camera pairs), RMS deviation of data sets from their own characteristics was $\Delta\epsilon_w = 0.0057$ across the range $0° \leqslant \theta \leqslant 85°$. When restricting the range to $0° \leqslant \theta \leqslant 60°$, the mean RMS deviation falls to $\Delta\epsilon_w = 0.0041$. Now, taking the RMS deviation of all data for APS TBC (all coupons, both cameras) from the overall best fit (data from all coupons and both cameras) we get values of $\Delta\epsilon_w = 0.0097$ and 0.0069 over the range $0° \leqslant \theta \leqslant 85°$ and $0° \leqslant \theta \leqslant 60°$, respectively.

The deviation of all individual data points from the overall best fit is shown in figure 7. We have already noted that the measurement difference between cameras (solid line in figure 7) is extremely small. RMS deviations from the overall best fit are approximately 1.7 times larger than RMS deviations from individual (per coupon, per camera) fits. With regard to EB-PVD TBC, we feel that the overall best fits for APS TBC are sufficiently good that they could be used in the majority of studies without the need for individual calibration (specific surface, specific camera through-calibration).

As we observed for the EB-PVD TBC coupons, we note that the scatter of the APS TBC data increases with increasing θ. This is likely due to increasing steepness of the $\epsilon_w(\theta)$ characteristic at high θ. We also note that coupon 10 has a notably higher emissivity at high ($\theta > 60°$) viewing angle (as measured by both cameras). The equivalent sand grain roughness height for coupon 10 ($k_S = 22.48$ μm) was almost double that for coupons 8 and 9 ($k_S = 15.60$ μm and $k_S = 14.84$ μm, respectively). We have noted the known positive correlation between surface roughness and emissivity, particularly at large θ (see [11]).

Finally, we consider the data for the three types of paint. For each type of paint, we tested a single coupon. Individual lines of best fit are shown in figure 4 (FLIR A665sc camera) and figure 5 (TIM640 camera). For the six individual characteristics (i.e. particular paint coupon, particular camera), the mean (across six paint coupon and camera pairs) deviation of the datasets from each characteristic was $\Delta\epsilon_w = 0.0033$ across the range $0° \leqslant \theta \leqslant 85°$. When restricting the range to $0° \leqslant \theta \leqslant 60°$, the mean RMS deviation falls to $\Delta\epsilon_w = 0.0026$. Now, taking the RMS deviation of all data for a particular paint coupon from the overall best fit for that coupon (i.e. data for both cameras for a single coupon), we get mean values of $\Delta\epsilon_w = 0.0052, 0.0035, 0.0029$ for Autotek, RS and NEXTEL paints, respectively, over the view-angle range $0° \leqslant \theta \leqslant 85°$. When restricting the angle range to $0° \leqslant \theta \leqslant 60°$, the mean deviations are reduced to $\Delta\epsilon_w = 0.0041, 0.0031, 0.0024$, respectively. The deviation of individual data points of a given paint type from the overall best fit for the same paint type is shown in figure 7. Deviations are small across the entire angle range. The difference in calibrations between the two cameras is also given in figure 7 for each paint type. We see that the differences between cameras is extremely small. For all three paint types, the RMS deviation from the overall best fit (data from two cameras) for a given paint type is approximately 1.2 times larger than the RMS deviations for an individual paint–camera pairing. This near-unity multiplier shows that the differences between cameras is small, allowing a single (common) calibration to be used with reasonable accuracy. We observe very mildly increasing scatter with increasing view angle. This is likely due to increasing steepness of the $\epsilon_w(\theta)$ characteristic at high θ.

4.3. Summary directional emissivity characteristics

We now present the key results of this paper, which are the summary directional emissivity characteristics for EB-PVD TBC, APS TBC, and three types of black paint. These characteristics are shown in figure 8. Equations of the form of equation (3) have been used to best fit all data (all coupons for a particular surface type; both cameras) for a particular surface type. The results are almost identical to those which would be achieved by averaging the individual characteristics for the two cameras—for a particular surface type—shown in figure 6. Best-fit coefficients a, b and c (for use with equation (3)) are presented in table 4. Coefficients of determination (so-called R-squared values) are also given.

First consider the best-fit characteristics for EB-PVD TBC and APS TBC. Both surface types have very high normal emissivity: for EB-PVD TBC we measure $\epsilon_w(0°) = 0.970$, and for APS TBC we measure $\epsilon_w(0°) = 0.966$. In the range $0° < \theta < 45°$, there was essentially no sensitivity of emissivity to the angle, with the ratio $\epsilon_w(\theta)/\epsilon_w(0°)$ taking values above 0.99 for both types of TBC. For $\theta > 45°$, we start to see angular sensitivity of ϵ_w with significant deviation from the normal emissivity values for $\theta > 60°$ and above. The angular sensitivity of EB-PVD TBC is greater than for APS TBC: this is likely due to the greater surface roughness of APS TBC, which delays emissivity reduction with the angle. The average roughness for APS TBC coupons was $k_S = 17.6$ μm; the average roughness for EB-PVD TBC coupons was $k_S = 3.96$ μm.

We now consider the best-fit characteristics for the three types of paint tested. The measured normal emissivity values for the Autotek VHT, RS matt, and NEXTEL Velvet paints were 0.933, 0.941 and 0.965, respectively: values in a similar

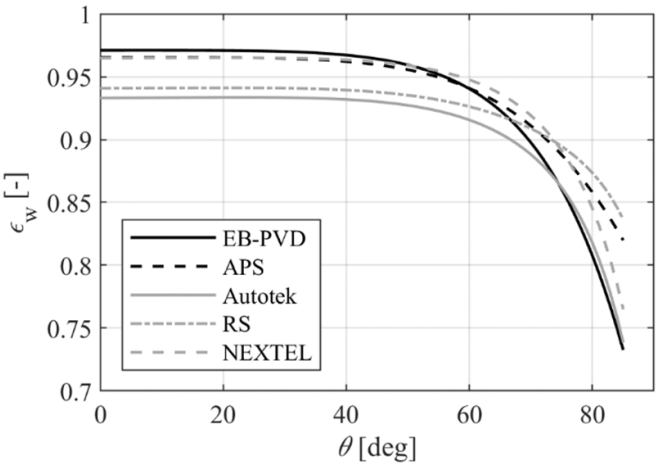

Figure 8. The overall best-fit directional emissivity characteristics for EB-PVD TBC, APS TBC, Autotek VHT black paint, RS matt black paint and NEXTEL Velvet paint.

Table 4. Coefficients (for use in equation (3)) associated with the overall best-fit characteristics of figure 8.

TBC	a (–)	b (–)	c (–)	R-squared (–)
EB-PVD TBC	1.411	7.4246×10^{-06}	0.1260	0.914
APS TBC	1.458	2.0331×10^{-05}	0.1171	0.943
Autotek VHT	1.699	1.3482×10^{-04}	0.0930	0.986
RS matt	1.644	9.7238×10^{-05}	0.0995	0.961
NEXTEL Velvet	1.462	7.3867×10^{-05}	0.1003	0.994

range to the TBC types tested. In the range $0° < \theta < 54°$, there was essentially no sensitivity of emissivity to the angle, with the ratio $\epsilon_w(\theta)/\epsilon_w(0°)$ taking values above 0.99 for all three types of paint. This is in agreement with the widely accepted approximation that variation in emissivity with the view angle is insignificant for view angles up to 55° for electrically non-conductive surfaces. For $\theta > 54°$, we start to see angular sensitivity of ϵ_w with significant deviation from the normal emissivity values for $\theta > 65°$ and above.

5. Conclusions

In this paper, we have presented detailed experimental measurements of the directional emissivity characteristics of a number of surface types common in gas turbine IR experiments: specifically, TBCs and high-emissivity paints. In total, five surface types were assessed: two types of TBC, and three types of high-emissivity paint. TBC samples were extracted as coupons from nozzle guide vanes from a modern production gas turbine engine. Measurements were conducted as through-calibrations with two different LWIR cameras: an FLIR A665sc camera; and a MicroEpsilon TIM640 camera. These cameras have different integration characteristics, allowing sensitivity to this effect to be determined. For the two types of TBC tested (EB-PVD TBC and APS TBC), several coupons per type were measured to determine the coupon-to-coupon scatter in the emissivity characteristics. Measurements were taken in the viewing angle range $0° \leqslant \theta \leqslant 85°$. Overall best fits to the data were performed using a modified version of the Fresnel emissivity equation. Coefficients for these best fits are provided to allow other researchers to use the measured emissivity characteristics. Detailed analysis of the data showed: very little difference in the through-calibrations for the two camera types used; high normal emissivities for all five surface types tested ($\epsilon_w(0°) = 0.970, 0.966, 0.933, 0.941$ and 0.965); insensitivity of emissivity to the viewing angle in the range $\theta < 45°$ for all five surface types; steep surface-specific decreases in emissivity with the viewing angle in the range $\theta > 60°$; and relatively limited difference between the emissivity characteristics for TBC samples of a particular type, allowing overall best-fit curves to be used in most cases with sufficient accuracy.

It is hoped that these data will be of practical value to the research community working on high-accuracy IR techniques.

Data availability statement

All data that support the findings of this study are included within the article (and any supplementary files).

Acknowledgment

The authors thank Dougal Jackson for his technical suggestions, Rolls Royce plc. for supplying parts, Ahren Sampath for his support with some experimental data collection, and the Oxford University LIMA service for supporting surface roughness measurements.

Author contributions

Matthew Stokes 0000-0001-8337-3176
Conceptualization (equal), Data curation (equal), Formal analysis (equal), Funding acquisition (supporting), Investigation (equal), Methodology (equal), Project administration (supporting), Validation (equal), Visualization (equal), Writing – original draft (lead), Writing – review & editing (equal)

Thomas Povey 0000-0001-8977-9644
Conceptualization (equal), Data curation (equal), Formal analysis (equal), Funding acquisition (lead), Investigation (equal), Methodology (equal), Project administration (lead), Supervision (lead), Validation (equal), Writing – original draft (equal), Writing – review & editing (equal)

Appendix A. Facility thermal model

A one-dimensional thermal model was used to determine the errors arising from: the assumption that the steady-state coupon surface temperature and copper-plate temperature (as

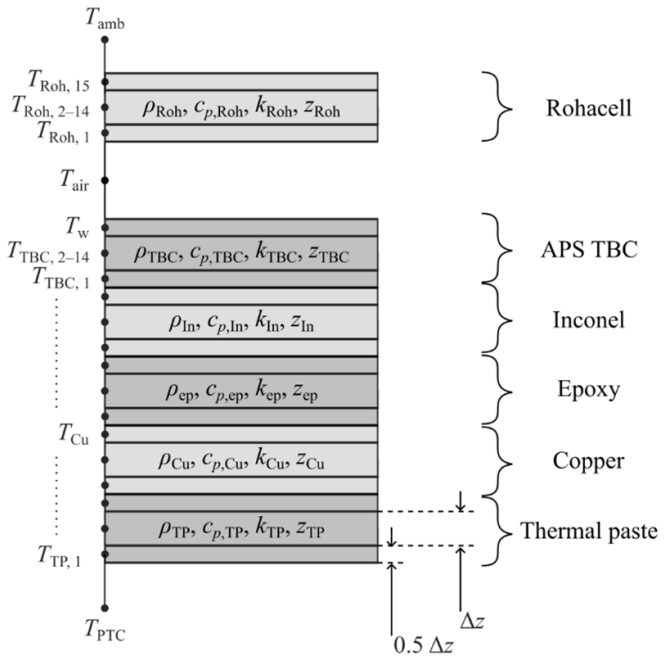

Figure A1. The low-order thermal model of the experimental facility.

Table A1. The physical properties used in the low-order thermal model.

Layer	z (mm)	ρ (kg m^{-3})	k (W m^{-1}K^{-1})	c_p (J kg^{-1}K^{-1})
Rohacell	30	71	0.03	1620
TBC	0.343	5000	0.7	450
Inconel	4	8440	15	435
Epoxy	0.2	4000	11	600
Copper	5	8940	420	385
Thermal paste	0.2	3000	6	800

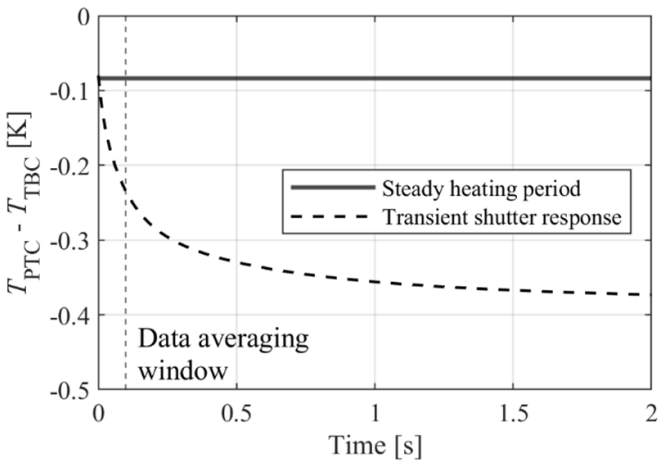

Figure A2. The temperature difference between the coupon surface and PTC heater in the steady state (after 45 min of heating) and in the transient period directly after the shutter opens.

measured by RTDs) are the same; the assumption that the *lapse* in coupon surface temperature in the 0.1 s period after the shutter opens (during which time data are acquired) is negligible.

We model the coupon with the greatest thermal resistance: coupon 10 has a layer of APS TBC of thickness $z = 343$ μm. The model (which represents the experimental setup; see figure 3) consists of six layers in the wall-normal direction; Rohacell (the outer shutter); an air gap; the APS TBC layer; Inconel; epoxy; the copper baseplate; and the thermal paste layer between the copper baseplate and the (assumed constant temperature) PTC heater. This is shown schematically in figure A1.

Each layer is discretised with 15 nodes in the through-wall direction. An explicit time-marching scheme was used to solve for each node temperature. Solutions were demonstrated to be independent of grid size and time step. Material properties (density ρ, specific heat capacity c_p, thermal conductivity k) and layer thicknesses are given in table A1.

On the bottom surface, a constant temperature boundary condition is set at the nominal PTC heater temperature $T_{PTC} = 378$ K. The outer surface of the Rohacell lid exchanges heat with the surroundings ($T_{amb} = 290$ K) through natural convection (heat transfer coefficient, $h_{nc} = 7$ W m^{-2} K^{-1}) and radiative heat transfer ($\epsilon_{roh} = 0.95$). The natural convective heat transfer coefficient is from an empirical correlation for the mean heat transfer coefficient on a vertical plate [12]. Convective heat transfer between the TBC top surface and the inner surface of the lid (heat transfer coefficient $h_{in} = 4$ W m^{-2} K^{-1}) is determined by an empirical correlation for flow in a vertical cavity with different sidewall temperatures [12]. Net radiative heat transfer in the enclosure cavity is also modelled. The temperature of the air in the enclosure (T_{air}) is determined from conservation of energy, assuming no losses and no mass transfer out of the enclosure volume.

The model is run to steady state (lid closed) to represent pre-heating, and also with the boundary conditions of the shutter opening (to see the temporal variation immediately afterwards). In this second mode, the Rohacell layer is removed from the model and the natural convective boundary conditions (h_{nc}) are applied directly to the upper TBC node. The differences between the heater temperature (T_{PTC}) and the surface node temperature (T_{TBC}) are plotted in figure A2 as a function of time, for both the steady-state (pre-heating) mode and the unsteady (directly after shutter opened) mode. After 45 min of heating, we see that the steady-state solution has a temperature difference $\Delta T = T_{PTC} - T_{TBC} = 0.08$ K. This is equivalent to an offset in emissivity of $\Delta\epsilon_w = 0.0015$ (results from perturbation of equation (2) at $\epsilon_w = 0.97$). The unsteady solution has an exponential decay from the steady state solution. We average data over a period of 0.1 s after the shutter opens. During this period, the unsteady solution has a mean temperature difference $\overline{\Delta T} = T_{PTC} - T_{TBC} = -0.17$ K. This is equivalent to an offset in emissivity of $\Delta\epsilon_w = 0.0028$, which is small compared to the estimated bias uncertainty of ϵ_w in our measurement.

Appendix B. Form of best-fit curves

For an optically smooth, opaque, electrically non-conductive surface, the theoretical variation in emissivity with the view angle is described by the Fresnel equations of reflectivity for S- and P-polarised light. The so-called Fresnel emissivity (ϵ_{F}) and reflectivity (ρ_{F}) are described by

$$\begin{aligned}\epsilon_{\mathbf{F}}(a,\theta) &= (1-\rho_{\mathbf{F}}(a,\theta)) \\ &= 1-\frac{1}{2}\left\{\left|\frac{\cos\theta-\sqrt{a^2-\sin^2\theta}}{\cos\theta+\sqrt{a^2-\sin^2\theta}}\right|^2+\left|\frac{a^2\cos\theta-\sqrt{a^2\sin^2\theta}}{a^2\cos\theta+\sqrt{a^2\sin^2\theta}}\right|^2\right\}.\end{aligned} \tag{B1}$$

where a is the refractive index of the surface. In this study, we determine curve fits of the form of equation (3) (rewritten here for clarity)

$$\epsilon_{\mathrm{w}}(\theta) = \epsilon_{\mathrm{F}}(a,\theta) + be^{c\theta} \tag{3}$$

where $be^{c\theta}$ is an additional exponential term to account for roughness-induced effects (based on theoretical modelling of specular reflection off rough surfaces [11]). Here, a, b, c are determined by non-linear least squares fitting of the data in MATLAB. The goodness of a particular fit is measured using the R-squared value of the curve fit to the underlying data.

References

[1] Witz G, Staerk K F, Maggi C M, Krasselt U and Bossmann H-P 2014 Burner rig testing of thermal barrier coatings for lifetime prediction *ASME Turbo Expo 2014* pp GT2014–25372

[2] Kirollos B, Lubbock R, Beard P, Goenaga F, Rawlinson A, Janke E and Povey T 2017 ECAT: an engine component aerothermal facility at the University of Oxford *ASME Turbo Expo 2017* pp GT2017–64736

[3] Yang G and Zhao C Y 2015 A comparative experimental study on radiative properties of EB-PVD and air plasma sprayed thermal barrier coatings *J. Heat Transfer* **137** 091024

[4] Eldridge J I, Spuckler C M, Street K W and Markham J R 2002 Infrared radiative properties of yttria–stabilized zirconia thermal barrier coatings *26th Annual Conf. on Composites, Advanced Ceramics, Materials, and Structures: B: Ceramic Engineering and Science Proc.*

[5] González-Fernández L, Del Campo L, Pérez-Sáez R B and Tello M J 2012 Normal spectral emittance of Inconel 718 aeronautical alloy coated with yttria stabilized zirconia films *J. Alloys Compd.* **513** 101–6

[6] Liebert C H 1978 Emittance and absorptance of the national aeronautics and space administration ceramic thermal barrier coating *Thin Solid Films* **53** 235–40

[7] Manara J, Brandt R, Kuhn J, Fricke J, Krell T, Schulz U, Peters M and Kaysser W A 2000 Emittance of Y2O3 stabilised ZrO2 thermal barrier coatings prepared by electron-beam physical-vapour deposition *High Temp.—High Press.* **32** 361–8 (available at: https://www.researchgate.net/publication/259573196_Emittance_of_Y2O3_Stabilised_ZrO2_Thermal_Barrier_Coatings_Prepared_by_Electron-Beam_Physical-Vapour_Deposition)

[8] Kirollos B and Povey T 2017 Laboratory infrared thermal assessment of laser-sintered high-pressure nozzle guide vanes to derisk engine design programs *J. Turbomach.* **139** 041009

[9] Kirollos B and Povey T 2017 High-accuracy infra-red thermography method using reflective marker arrays *Meas. Sci. Technol.* **28** 095405

[10] Bons J 2005 A critical assessment of Reynolds analogy for turbine flows *J. Heat Transfer* **127** 472–85

[11] Wen C-D and Mudawar I 2006 Modeling the effects of surface roughness on the emissivity of aluminum alloys *Int. J. Heat Mass Transfer* **49** 4279–89

[12] Incropera F P, DeWitt D P, Bergman T L and Lavine A S 1996 *Fundamentals of Heat and Mass Transfer* (Wiley)